The Global Atmospheric Circulation Response to Tropical Diabatic Heating Associated with the Madden–Julian Oscillation during Northern Winter

KYONG-HWAN SEO

Department of Atmospheric Sciences, Pusan National University, Busan, South Korea

SEOK-WOO SON

Department of Atmospheric and Oceanic Sciences, McGill University, Montreal, Quebec, Canada

(Manuscript received 4 October 2010, in final form 10 August 2011)

ABSTRACT

The detailed dynamical mechanisms of the upper-tropospheric circulation response to the Madden–Julian oscillation (MJO) convection are examined by integrating a primitive equation model. A series of initial-value calculations with the climatological boreal winter background flow forced by the MJO-like thermal forcing successfully capture the key aspects of the observed circulation response to the MJO convection. This suggests that a large fraction of MJO-related circulation anomalies are direct responses to tropical heating in both the tropics and extratropics and can be largely explained by linear dynamics.

It is found that MJO-like dipole heatings not only intensify tropical upper-tropospheric anomalies but also weaken them at certain regions because of the interaction between equatorial Kelvin and Rossby waves. The Rossby wave train primarily excited by horizontal divergence of upper-level perturbation flow propagates northeastward and then heads back to the equator. In this way, Rossby wave activity once generated over the subtropical Indian Ocean tends to enhance the equatorial upper-tropospheric anomalies over the tropical Atlantic and West Africa that have already been created by the zonally propagating equatorial Rossby and Kelvin waves. A ray path tracing reveals that a successive downstream development of Rossby wave train mostly results from the large-scale waves with zonal wavenumbers 2–3 in the Northern Hemisphere and 3–5 in the Southern Hemisphere.

The sensitivity tests show that the overall results are quite robust. It is found, however, that the detailed circulation response to the MJO-like forcing is somewhat sensitive to the background flow. This suggests that MJO-related circulation anomalies may have nonnegligible long-term variability and change as background flow varies.

1. Introduction

The Madden–Julian oscillation (MJO) is the most dominant physical mode of tropical intraseasonal variability with a characteristic time scale of 30–70 days (Madden and Julian 1972). Previous studies have found that the tropical diabatic heating associated with the MJO induces the atmospheric circulation anomalies in both the tropics and extratropics (e.g., Matthews et al. 2004; Lin et al. 2006, and references therein). The teleconnection to the extratropics occurs in the form of a Rossby wave train, which is characterized by the northeastward propagation from the vicinity of the heating source, the subsequent reflection of the wave at a turning latitude located at higher latitudes, and the southeastward propagation to the tropics. The resulting circulation anomalies then impact surface air temperature and rainfall variations over Asia, the North Pacific, North America, the tropical eastern Pacific, and the Atlantic (e.g., Higgins et al. 2000; Jones and Schemm 2000).

A large portion of the global circulation variability in the upper troposphere is accounted for by the MJO. In fact, Matthews et al. (2004) have estimated that the fraction of variance of the upper-level (200 hPa) circulation that is explained by the MJO is as much as 70% in the tropics and 35%–40% in the Northern Hemisphere (NH) extratropics although this fraction falls below 20% for the Southern Hemisphere (SH) extratropics. Therefore, it is required to correctly understand and simulate

Corresponding author address: Dr. Kyong-Hwan Seo, Department of Atmospheric Sciences, Pusan National University, Busan, South Korea.
E-mail: khseo@pusan.ac.kr

DOI: 10.1175/2011JAS3686.1

the MJO and its dynamics in order to better predict long-term weather both in the tropics and extratropics. The attribution and prediction of global atmospheric circulation variability is one of the most useful applications in meteorology and climate, so the detailed dynamical processes associated with the formation of statistically significant circulation anomaly signals should be investigated.

The current generation of atmospheric general circulation models (GCMs) and atmosphere–ocean coupled GCMs struggles in properly simulating and forecasting the MJO (Hendon 2000; Inness and Slingo 2003; Sperber et al. 2005; Lin et al. 2006; Seo et al. 2005, 2007, 2009; Seo and Wang 2010; Fu et al. 2008). Lin et al. (2006) have shown that only 2 coupled GCMs [i.e., ECHAM (European Centre for Medium-Range Weather Forecasts and Hamburg) and the Centre National de Recherches Météorologiques (CNRM)] out of 14 coupled models participating in the Intergovernmental Panel on Climate Change (IPCC) Fourth Assessment Report (AR4) can produce convective variances in the intraseasonal band that are similar to those observed. However, further analysis of those models' capability for reasonable MJO simulation reveals a lack of coherent eastward propagation of intraseasonal convective anomalies across the Maritime Continent and western Pacific (not shown)—a feature ubiquitous to many contemporary coupled models (e.g., Slingo et al. 1996; Seo et al. 2009; Seo and Wang 2010). Seo and Wang (2010) recently showed that the Climate Forecast System model, which is an operational coupled model of the National Centers for Environmental Prediction (NCEP), produces much improved MJO simulation when a relaxed Arakawa–Schubert cumulus scheme (Moorthi and Suarez 1992, 1999) is used. This is mainly because model precipitation has reasonable sensitivity to environmental humidity (Derbyshire et al. 2004), and the top-heavy vertical heating profile arising from convective detrainment of moisture to the environment and stratiform heating acts to sustain the MJO by creating eddy available potential energy and a moisture–stratiform instability feedback process (Mapes 2000; Kuang 2008; Fu and Wang 2009). The 200-hPa circulation pattern in response to the model MJO convection is markedly improved in this model, possibly enhancing the predictability of circulation variability, even for the extratropics.

The global circulation response to tropical heating has been often investigated by integrating GCM with prescribing monopole heating that represents the effect of a warm pool sea surface temperature (SST) or anomalous east-central Pacific SST warming associated with an El Niño event (Sardeshmukh and Hoskins 1988; Jin and Hoskins 1995; Ashok et al. 2007b) or boreal summer Asian monsoon-related convective perturbations (Lin 2009). In those studies, especially those based on initial value calculations, extratropical circulation response is regarded as a Rossby wave response to tropical diabatic heating and often understood through the nondivergent barotropic wave dispersion theory (e.g., Hoskins and Karoly 1981; Hoskins and Ambrizzi 1993). The upper-troposphere anomalous divergence in regions of tropical heating is found to act as a Rossby wave source (RWS) for poleward dispersing extratropical wave activity (Sardeshmukh and Hoskins 1988; Lin 2009). Numerical experiments have been also performed with the MJO-like forcing, which retains a dipole (or tripole in some phases) heating structure. Matthews et al. (2004) showed that the tropical circulation anomalies form as a forced equatorial Rossby and Kelvin wave response to the MJO heating. The extratropical circulation anomalies were shown to be a result of the direct response to MJO heating, rather than a triggering and growth of unstable barotropic normal modes in the extratropics (Borges and Sardeshmukh 1995). In their initial-value calculations, however, the modeled circulation anomalies were erroneously shifted westward by about 20° longitude relative to the observations, and for the tropical anomalies a detailed mechanism of interaction between equatorial Rossby and Kelvin waves due to the dipole heating was not explored. The enhanced and suppressed convections are only separated by 80° longitude so they are expected to produce a more or less complicated Rossby and Kelvin wave interaction, such as an interfering or intensifying effect between them.

By extending and updating previous studies (e.g., Matthews et al. 2004), we present herein improved simulations of the global circulation response to MJO forcing and a more in-depth analysis on the mechanism. A series of initial-value calculations are performed by integrating a dynamical core GCM with MJO-like thermal forcing on the climatological background flow. Simulation results are then understood with equatorial wave dynamics and nondivergent barotropic Rossby wave dynamics in the extratropics. For instance, the formation of an extratropical circulation response is investigated by using a ray-tracing technique for Rossby wave propagation (Hoskins and Karoly 1981; Branstator 1983; Karoly 1983; Hoskins and Ambrizzi 1993). This will elucidate the zonal scales of Rossby waves that are able to disperse from the heating area, travel to the northern and southern extratropics, and propagate back to the tropical region. In addition, the RWS associated with the MJO dipole forcing, which has not been examined previously, will be presented. It will be shown that an asymmetric RWS pattern arises between the heating over the Indian Ocean and the cooling over the western Pacific.

The sensitivity tests to the amplitude and vertical structure of forcing, model internal diffusion, and background flow are also performed. In particular, to understand interannual variability of MJO-induced circulation changes in the extratropics, initial-value integrations are also performed for El Niño and La Niña basic states. The possible impact of the MJO on the extratropical circulation in a warm climate is also discussed.

2. The data and model

a. The data and observed MJO structure

To represent deep convection in the tropics, daily outgoing longwave radiation (OLR) from the Advanced Very High Resolution Radiometer (AVHRR) onboard the National Oceanic and Atmospheric Administration (NOAA) polar-orbiting satellites (Liebmann and Smith 1996) is used for the 28-yr period from 1979 to 2006. Other dynamic and mass fields, including daily mean zonal and meridional winds, are obtained from the NCEP–National Center for Atmospheric Research (NCAR) reanalysis (Kalnay et al. 1996) for the same 28-yr period. Streamfunction and divergence are calculated from the horizontal wind fields. Both datasets are stored on the same 2.5° × 2.5° longitude–latitude grid. The anomaly field for each variable is derived by removing the annual cycle, which is composed of the time mean and first three annual harmonics, from the total field at each grid point. To capture the intraseasonal variations, the anomaly field is subjected to 20–90-day bandpass filtering using a Lanczos filter. Only the winter season [i.e., December–February (DJF)] is considered.

To identify the most dominant evolution patterns of the MJO, an empirical orthogonal function (EOF) analysis is performed on the intraseasonally filtered AVHRR OLR. This results in the two leading well-known EOF modes statistically distinct from the other higher modes. The first EOF has a strong convective cloud centered over the Maritime Continent and the western Pacific (110°–150°E) and the second has one over the Indian Ocean from 70° to 110°E [not shown here, but they can be seen in previous literature; e.g., in Matthews et al. (2004) and Seo et al. (2005)]. Their principal components (PCs) are significantly correlated at about 10–12-day lag (not shown), and hence these modes in combination represent the typical eastward-propagating MJO convective signal. Using these two EOF modes and PCs, an evolution cycle is constructed with eight different phases according to the location of the enhanced MJO convection as shown in Wheeler and Hendon (2004). Then, composite OLR anomaly fields are constructed for the strong MJO events where their PC amplitude (i.e., $\sqrt{PC1^2 + PC2^2}$) is greater than 2.0 for each MJO phase. Figure 1 shows the composite OLR anomaly fields for phases 1–4. The remaining phases (5–8) are nearly the same as Fig. 1 with only a sign reversal. Considering the strongest MJO signal appears at the period of about 48 days (e.g., Matthews 2000; and others), the time difference between each phase is approximately 6 days. This convective structure is used to construct an idealized MJO diabatic heating field that forces the simple GCM described below.

b. The model and experiment design

To assess whether the global atmospheric circulation anomalies arise as a direct response to MJO convective heating and to investigate the dynamical mechanisms, initial-value calculation is performed by using a primitive equation model based on the dynamical core of the Geophysical Fluid Dynamics Laboratory (GFDL) atmospheric GCM (Gordon and Stern 1982). The dynamical core model has a rhomboidal 30 (hereafter R30) resolution in the horizontal and 20 equally spaced sigma σ levels that change from 0.975 to 0.025. This model is initialized about a DJF climatological basic state, which contains three-dimensional wind, temperature, and surface pressure fields (no moisture), and integrated up to 30 days as in Jin and Hoskins (1995). To prevent the basic state from being drifted, a forcing term is applied during the model integration. The dissipation terms used in the model run include a vertical diffusion with a coefficient of 0.5 $m^2\ s^{-1}$ and an eighth-order horizontal diffusion with a coefficient of $8 \times 10^{37}\ m^8\ s^{-1}$ (Son and Lee 2005). A series of tests have shown negligible sensitivity to changes in the values and orders of the horizontal diffusion coefficient.

To mimic MJO forcing, external thermal forcing is added to the temperature tendency equation while all other fields are kept as they are. The external forcing is smoothly turned on from $t = 0$ to $t = 2$ days to avoid an undesirable generation of gravity waves, and after that the heating with a full strength (which will be shown in Fig. 3) persists. The heating anomaly assumes an elliptical form in the horizontal with a maximum or minimum center at the equator, as in Ting and Held (1990):

$$\delta Q(\lambda, \phi) = \{A_1 e^{-[(\lambda-\lambda_1)/L_x]^2} - A_2 e^{-[(\lambda-\lambda_2)/L_x]^2} + A_3 e^{-[(\lambda-\lambda_3)/L_x]^2}\} \times e^{-(\phi/L_y)^2}, \quad (1)$$

where λ and ϕ represent longitude and latitude, and L_x and L_y the longitudinal and latitudinal scales, respectively. Also, A_1, A_2, and A_3 are the amplitudes of the heating/cooling at the longitudinal locations of enhanced or suppressed convection centers λ_1, λ_2, and λ_3, respectively. Figure 2 shows the heating anomalies forced to derive the circulation response in the model for each MJO phase. They are designed to mimic the observed OLR

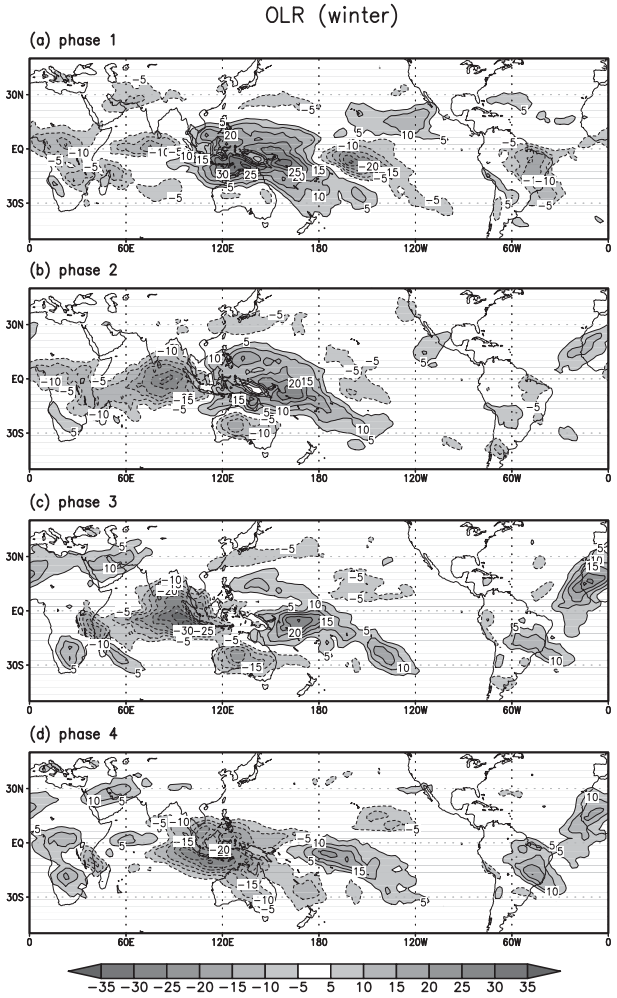

FIG. 1. Composite AVHRR OLR anomaly fields during winter for the first four phases. Phases 5–8 are similar to phases 1–4 with a sign reversal (so they are omitted). The composite fields are constructed for the cases where the normalized MJO amplitude is greater than 2.0. The contour interval is 5 W m^{-2}. The dotted (solid) lines denote enhanced (suppressed) convection. The time interval between two phases is ~6 days.

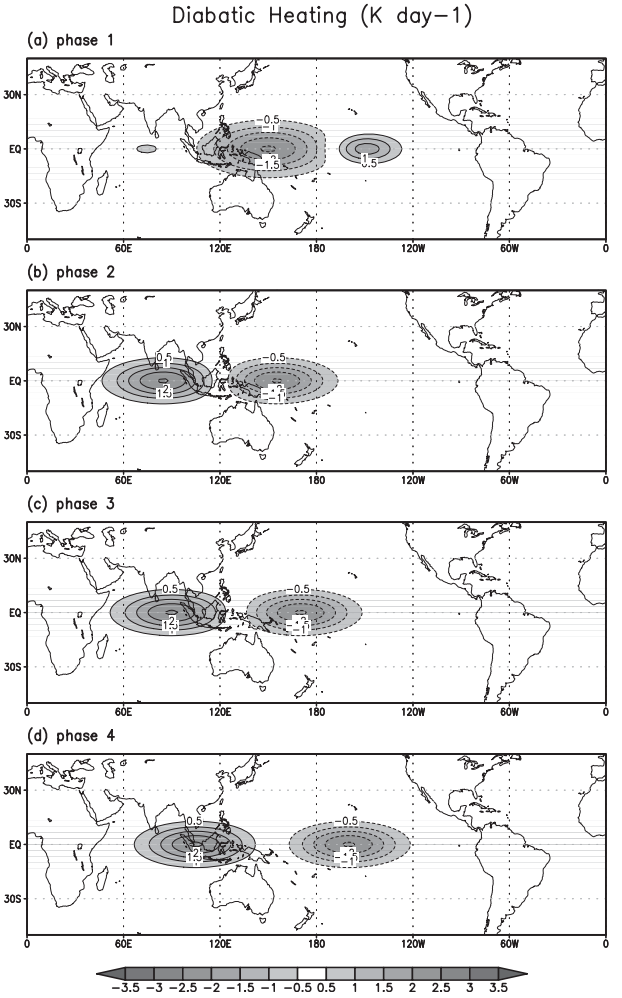

FIG. 2. Diabatic heating imposed in each model simulation for phases 1–4. It mimics the observed composite OLR anomaly fields in Fig. 1. Phases 2, 3, and 4 have a dipole convective forcing, but phase 1 has a weak tripole forcing. The contour interval is 0.5 K day^{-1}. The solid (dotted) lines denote positive (negative) heating.

anomalies shown in Fig. 1. For phase 1, A_1, A_2, and A_3 are specified nonzero but for phases 2, 3, and 4, which have a dipole forcing, A_3 sets to zero. The vertical heating profile is in the form of $(1-\sigma)\sin[\pi(1-\sigma)]$ with a peak heating rate of 2.5 K day^{-1} at $\sigma = 0.35$ as shown in Fig. 3. A vertically averaged heating rate is approximately 1.4 K day^{-1}, which is equivalent to latent heating that produces 5–6 mm of precipitation per day (e.g., Jin and Hoskins 1995). This precipitation rate is consistent with the observed strong MJO events as shown in the Climate Prediction Center (CPC) Merged Analysis of Precipitation (CMAP) data and the Tropical Rainfall Measuring Mission (TRMM) precipitation radar data (see Figs. 3 and 8, respectively, of Lin et al. 2004). The same vertical profile has been used in the study of the global extratropical circulation response to the diabatic heating of the Asian summer monsoon by Lin (2009).

3. Results

a. Observed global circulation response to MJO forcing

First, the observed global circulation patterns induced by MJO convective forcing are examined using 200-hPa streamfunction anomalies for the first half of a cycle (i.e., phases 1–4) (Figs. 4a–d). As mentioned in the previous section, the upper-level circulation anomalies are composited with respect to the strong MJO events whose amplitude, measured by the values of the first two normalized PCs, is greater than 2 (which signifies the upper

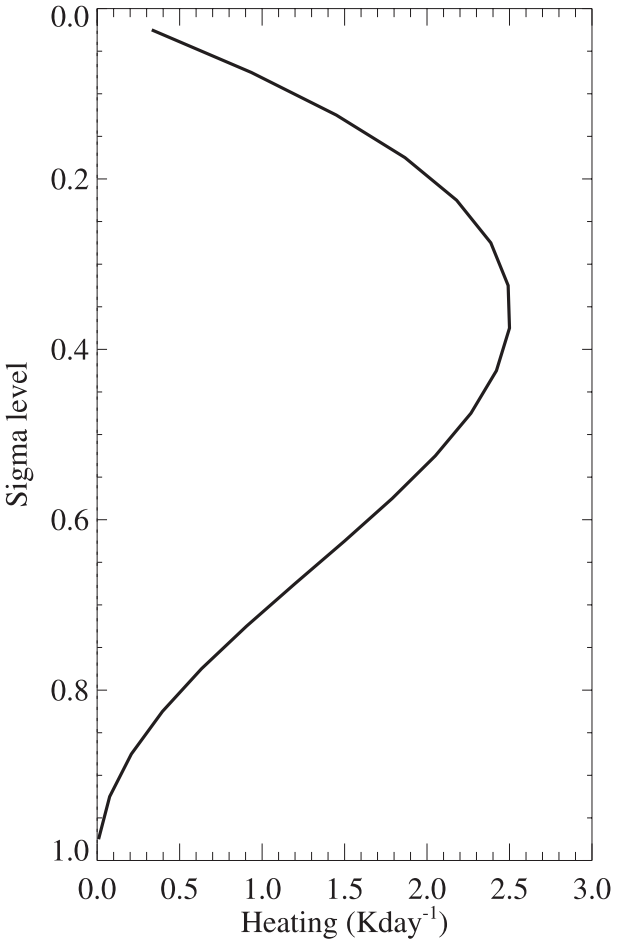

FIG. 3. Vertical heating profile at the maximum heating location.

5% strong events). This procedure is basically identical to the regression of streamfunction anomalies against a deviation of PC1 = 2 and PC2 = 2, as in Matthews et al. (2004) and Seo and Wang (2010). As MJO convection anomalies develop over the Indian Ocean and propagate to the east, the circulation response also propagates to the east. Phase 1 has a large suppressed convective center over the western Pacific (see Fig. 2a) and as a response to this forcing (Fig. 4a), a cyclonic flow couplet off the equator appears across the tropical region of the Eastern Hemisphere. The off-equatorial circulation anomalies are located to the west of (or collocated with) the convective anomaly (Gill 1980; Jin and Hoskins 1995). Along with this, the easterly anomalies appear along the equator to the east of this forcing, indicating the establishment of the Rossby and Kelvin wave circulation response (e.g., Matthews 2000; Seo and Kim 2003; Seo and Wang 2010). The enhanced convection (although weak) located to the east of the date line also forms a tropical anticyclonic couplet straddling the equator and a Kelvin wave response characterized by the equatorial westerly anomaly near 60°W.

At phase 2 (or equivalently 6 days later) (Fig. 4b), as enhanced convection develops over the Indian Ocean, anticyclonic Rossby waves appear off the equator to the west of heating and due to these waves, the cyclonic off-equatorial wave response to the suppressed convection over the western Pacific is greatly constrained in the zonal extent (cf. Figs. 4a and 4b in the Eastern Hemisphere). A strong heating also excites Rossby wave train to the extratropics as evident in the NH. The overall structure becomes more prominent at phase 3 (Fig. 4c). For instance, anticyclonic anomalies at 45°N, 170°E are strengthened about 3 times from phases 2 to 3. During these two phases, easterly anomalies along about 30°–35°N over 140°E–160°W (the boundary between the subtropical cyclonic anomaly and extratropical anticyclonic anomaly) act to weaken the Asian–Pacific jet and retract it to the west (Matthews et al. 2004). In remote places, extratropical circulation anomalies also develop over western Canada (at phases 2 and 3) and eastern Canada (at phase 3), forming a wave train emanating from the upstream tropical region to the higher latitudes with a resemblance to the Pacific–North American (PNA) teleconnection pattern (although it is not identical). Phase 3 shows a more conspicuous wave train over the PNA region and even eastern Atlantic, seemingly along a great circle (Fig. 4c). Phase 4 shows a similar circulation response to that of phase 3 but with a slightly eastward shift in the tropical circulation pattern (Fig. 4d).

There is a weak hint of a wave train in the SH. For example, at phases 2 and 3, waves coming from the equatorial Indian Ocean disperse across the southern Indian Ocean and southern Pacific in a counterclockwise sense. Their wavelength appears to be shorter than that of the Rossby wave train in the NH. This feature will be explained by comparing the model simulation results described below.

b. Model results

The observed circulation anomalies induced by the MJO convective forcing exhibit distinct patterns in both the tropics and extratropics. Do these anomalies arise from a direct dynamic response to the MJO convective heating? To address this question and to better understand the dynamical processes, a series of dynamic-core GCM experiments are performed. Again, the model fields are driven by a steady diabatic forcing and integrated for 30 days for each phase. The model tends to respond almost linearly to the imposed forcing until about 15 days, after which unstable waves with eastward phase speed and group velocity dominate the model fields (refer to Fig. 7d). This characteristic is quite typical and has been

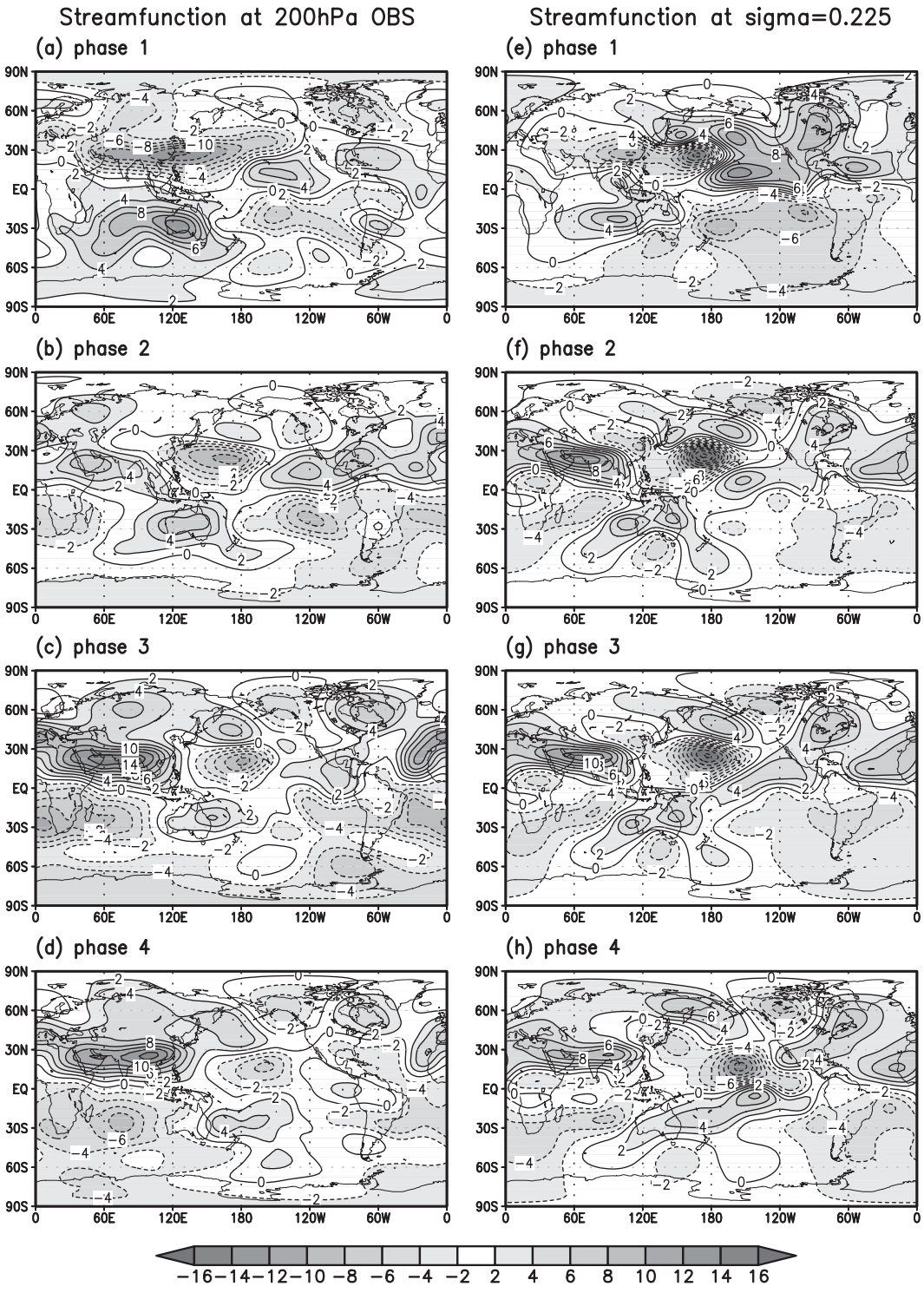

FIG. 4. (a)–(d) Observed DJF composite 200-hPa streamfunction anomalies for phases 1–4 and (e)–(h) upper-troposphere ($\sigma = 0.225$) streamfunction anomalies at day 15 of model simulations with forcings presented in Fig. 2. The contour interval is 2.0×10^6 m^2 s^{-1}. Positive (negative) values represent clockwise (counterclockwise) rotations.

reported in previous studies (Jin and Hoskins 1995; Matthews et al. 2004; Lin 2009). As we are mainly interested in the linear (or direct) responses of atmospheric circulation to MJO-like thermal forcing, model results up to day 15 are analyzed in this study. Only anomalies, deviations from the climatology (i.e., the basic state), will be shown.

Figures 4e–h present streamfunction anomalies in the upper troposphere ($\sigma = 0.225$) at day 15 for each phase. Phase 1 (Fig. 4e) exhibits two pairs of the cyclonic and anticyclonic couplets to the west and east, respectively, of the date line, similar to the observations. The zonal extent of the cyclonic anomaly over Asia is somewhat narrower than in the observations, whereas the anticyclonic anomaly over tropical Atlantic is reasonably well captured. In the extratropics, model simulations show more prominent wave trains over North Pacific than in the observations. Their wavelength is shorter, resulting in an opposite-signed streamfunction anomaly over eastern Canada. Note that significant streamfunction response over the North Pacific arises from the Rossby wave response to the negative forcing located over the western Pacific. Once the MJO convection develops over the Indian Ocean, the extratropical response is greatly improved (Fig. 4f). This includes the proper simulations of an anticyclonic anomaly over the North Pacific and a cyclonic anomaly farther to the north. The model tropical response also matches the observation well. All of these results indicate that the circulation anomalies are mainly due to a direct response to the MJO-related diabatic heating.

Phases 3 and 4 also show streamfunction anomalies that are similar to those observed in both the tropics and extratropics (Figs. 4g,h). The cyclonic and anticyclonic couplets about the equator are well simulated with a reasonable range of amplitudes, especially in phase 3. In phase 3, even the downstream positive streamfunction anomalies over Central America and the eastern Atlantic–western Africa and the negative anomaly near South America in the Western Hemisphere are very similar to the observation. The circulation anomaly pattern over the tropical Atlantic is also well captured in phase 4. The extratropical circulation anomalies in both phases 3 and 4 are significantly well reproduced, showing the prominent north-northeast–southeastward directing wave train in the NH, which appears to be characterized by a zonal wavenumber 3. The SH extratropical anomalies exhibit more pronounced and organized wave train than the observed ones. This exaggeration, however, provides a helpful insight into the interpretation of the observed circulation anomalies such as the positive anomalies, although weak, at about 60°S, 180° in phase 3 (Fig. 4g), and the negative and positive anomalies along 60°S at 150°E and 150°W, respectively, in phase 4 (Fig. 4h).

TABLE 1. Pattern correlations between the observed and modeled streamfunction anomalies for selected domains for phases 1–4. Correlation coefficients for the upper troposphere are from day-15 model integration fields. All calculated correlation coefficients are statistically significant at the 95% level except for the domain [30°–90°S] of phase 1. A Student's t test is used and the effective degree of freedom is calculated using the method of Ebisuzaki (1997).

Domain	Upper troposphere ($\sigma = 0.225$)
Globe	Phase 1: 0.57
	Phase 2: 0.74
	Phase 3: 0.77
	Phase 4: 0.60
30°S–30°N	Phase 1: 0.72
	Phase 2: 0.75
	Phase 3: 0.78
	Phase 4: 0.61
30°–90°N	Phase 1: 0.46
	Phase 2: 0.71
	Phase 3: 0.71
	Phase 4: 0.50
30°–90°S	Phase 1: 0.28
	Phase 2: 0.67
	Phase 3: 0.59
	Phase 4: 0.53

Again, all these features suggest that the tropical and extratropical circulation anomalies arise primarily from a direct response to the MJO heating. Table 1 shows the pattern correlations between the observed and modeled streamfunction anomalies for each phase. As can be seen, the correlation is greatest (0.77) at phase 3 among the different phases for the global region. This is also true for the tropics and northern extratropics. Phase 1 has the lowest pattern correlation due to the lack of coherence in the extratropics in the NH. In the tropics where the direct circulation response to tropical MJO heating occurs, the correlations are highest among the different domains. In general, the correlations of the southern extratropics are lower than those of the northern counterpart.

The corresponding lower-tropospheric ($\sigma = 0.875$) streamfunction anomalies at day 13 show a rich structure (Fig. 5), which is in fact expected because of the growth of unstable baroclinic synoptic-scale waves in the lower troposphere earlier than in the upper level in the model integrations (Jin and Hoskins 1995). Although the spatial scale of the simulated anomalies is relatively smaller than the observation, the gross feature is properly reproduced by the model simulations. For instance, the formation of cyclonic (anticyclonic) Rossby wave couplets across the equator and westerly (easterly) Kelvin wave driven by enhanced (suppressed) convection is qualitatively well captured. The pattern correlation coefficients are found to be 0.44–0.68 over the globe with the weakest correlation during phase 1 and the strongest correlation during phase 3.

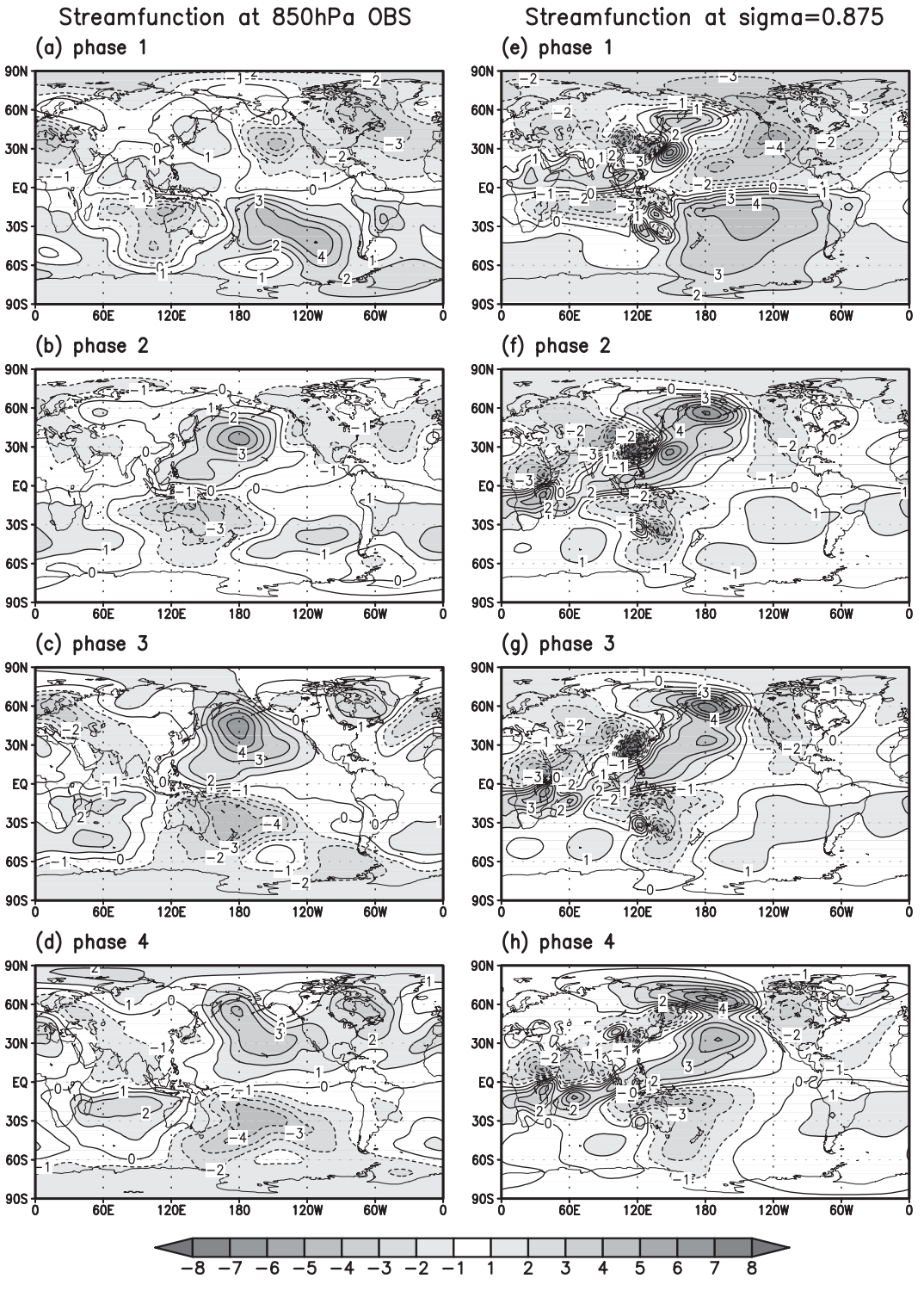

FIG. 5. As in Fig. 4, but (a)–(d) at 850 hPa and (e)–(h) for the lower troposphere ($\sigma = 0.875$) streamfunction anomalies at day 13. The contour interval is 1.0×10^6 m^2 s^{-1}.

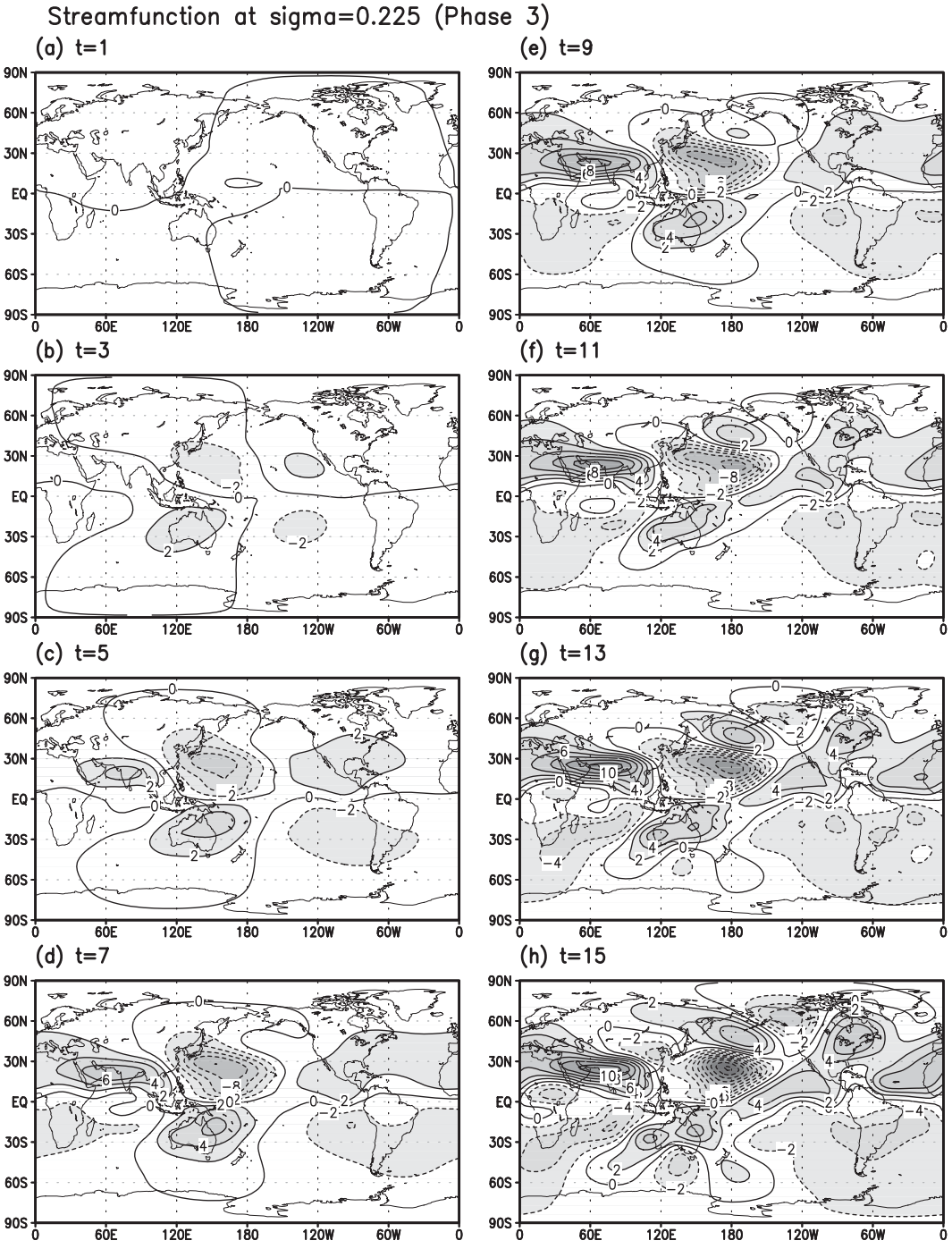

FIG. 6. Evolution of the upper-troposphere ($\sigma = 0.225$) streamfunction anomalies in the model simulation with MJO phase-3 forcing (Fig. 2c).

The vertical structure of the anomalies is also reasonably well captured. In general, the lower-tropospheric response is almost opposite to the upper-troposphere response in the tropics, signifying a baroclinic structure in the tropics (Figs. 4 and 5; Gill 1980). By contrast, extratropical circulation response is to a large degree equivalent barotropic, especially in the latitudes higher than 45°. These characteristics are qualitatively well reproduced by the model simulations.

To determine how the global circulation anomalies are formed during the integrations, Fig. 6 shows the upper-troposphere ($\sigma = 0.225$) model streamfunction anomaly

for phase 3 from days 1 to 15. Equatorial response appears immediately as the tropical forcing is switched on (Figs. 6a,b). By day 3, to the east of the date line, a pair of anticyclones is generated by equatorial Kelvin waves that are directly induced by the suppressed convection over the western Pacific. The cyclonic circulation couplet about the equator to the west of the date line is formed by both a Rossby wave response to the suppressed convection over the western Pacific and a Kelvin wave response to the enhanced convection over the Indian Ocean. Subtropical Rossby waves near 60°E are not explicitly formed until days 5 and 7 (Figs. 6c,d). By day 7, the subtropical circulation anomalies induced by Kelvin waves in the Western Hemisphere spread eastward and ultimately meet the westward propagating Rossby waves over the Arabian Sea and southern Africa, forming a very broad anticyclonic flow region. The major tropical features are therefore established in about one week, consistent with previous studies (e.g., Jin and Hoskins 1995).

The extratropical wave train pattern is then formed in the second week (Figs. 4e–h). The circulation anomalies over the North Pacific and eastern Canada strengthen during the integration and even the wave train appears to direct southeastward into the tropical Atlantic and West Africa. This result clearly demonstrates that the tropical circulation anomalies in the Western Hemisphere are formed by combined effects of the tropically trapped Rossby and Kelvin waves and the midlatitude Rossby wave train (as will be discussed in detail in the next section). In the SH, wave train also develops in the vicinity of Australia by days 13–15 (Figs. 6g,h), with the observed composite circulation pattern in this region (Fig. 4c) being somewhat similar to that of Fig. 6g. Since the model integration at phase 3 shows the highest pattern correlation and a clear midlatitude wave train, a ray-tracing method following the wave's group velocities will be applied at this phase to present a clearer view of the wave train path in the next section.

To visualize interactions between the equatorially trapped Rossby and Kelvin waves, the time evolution of geopotential height anomalies averaged over 5°S and 5°N is presented in Fig. 7. Here the geopotential height anomaly is considered since its sign does not change across the equator, whereas that of streamfunction anomalies changes about the equator because of the involvement of the Coriolis parameter. To identify the relative importance of the heating at 90°E and the cooling at 170°E, two additional experiments are carried out (i.e., one with a monopole heating at 90°E and the other with a monopole cooling at 170°E). Results are presented in Figs. 7b,c. Linear combination of these two experiments is quantitatively similar to the reference run until day 15 as evident in Fig. 7d. A nonlinear growth, however, emerges afterward due to the development of unstable waves.

The monopole heating and cooling respectively generate positive and negative geopotential height anomalies over the broad regions of the tropics as they propagate both eastward and westward in accordance with equatorial Kelvin and Rossby waves (Figs. 7b,c). As can be inferred from contour slopes, eastward-propagating Kelvin waves are about 3 times faster than the westward-propagating Rossby waves as in the observations. In the reference run (Fig. 7a), both positive and negative anomalies are generated by the heating–cooling dipole and cancel each other. For instance, the Kelvin wave response to the heating at 90°E (positive anomalies) is offset by the Rossby wave response to the cooling at 170°E (negative anomalies). Likewise, the Rossby wave response to the heating and the Kelvin wave response to the cooling are mixed up to the west of the heating. It occurs as Kelvin waves take only 6 or 7 days to reach the Indian Ocean while the Rossby wave slowly propagates westward from the heating center. As a result, the equatorial waves propagating in an opposite direction from the dipole heating oppose each other and prevent the equatorial positive or negative geopotential height anomalies from growing, resulting in successive wobbling of positive (negative) anomalies around 100°E (180°) with time. An additional experiment using a dipole heating centered at 90°E and 90°W (not shown) facilitates the above feature by separating the dipole forcing to a greater distance so that the anomaly propagation by Rossby waves is more clearly seen.

c. *Model results: Rossby wave ray tracing*

As stated above, once the Rossby wave train is generated by the enhanced convection over the Indian Ocean, it apparently affects extratropical circulations. To better understand this teleconnection, a ray tracing is performed to the model output of phase 3 by using the nondivergent barotropic Rossby wave theory of Hoskins and Karoly (1981) and Hoskins and Ambrizzi (1993). In brief, a dispersion relationship for barotropic Rossby wave perturbations to a basic zonal flow $\overline{U}$ on a β plane is given as

$$\omega = \overline{U}k - \frac{\beta_* k}{K^2}, \tag{2}$$

where $K^2 = k^2 + l^2$ (the square of the total wavenumber), with k and l being zonal and meridional wavenumbers, respectively, and $\beta_* = \partial f/\partial y - \partial^2 \overline{U}/\partial y^2$. The omitted definitions of the variables in the equations follow their usual meaning or convention in atmospheric sciences. For varying zonal wavenumber, meridional wavenumbers are calculated from the dispersion relationship [(2)] and thus

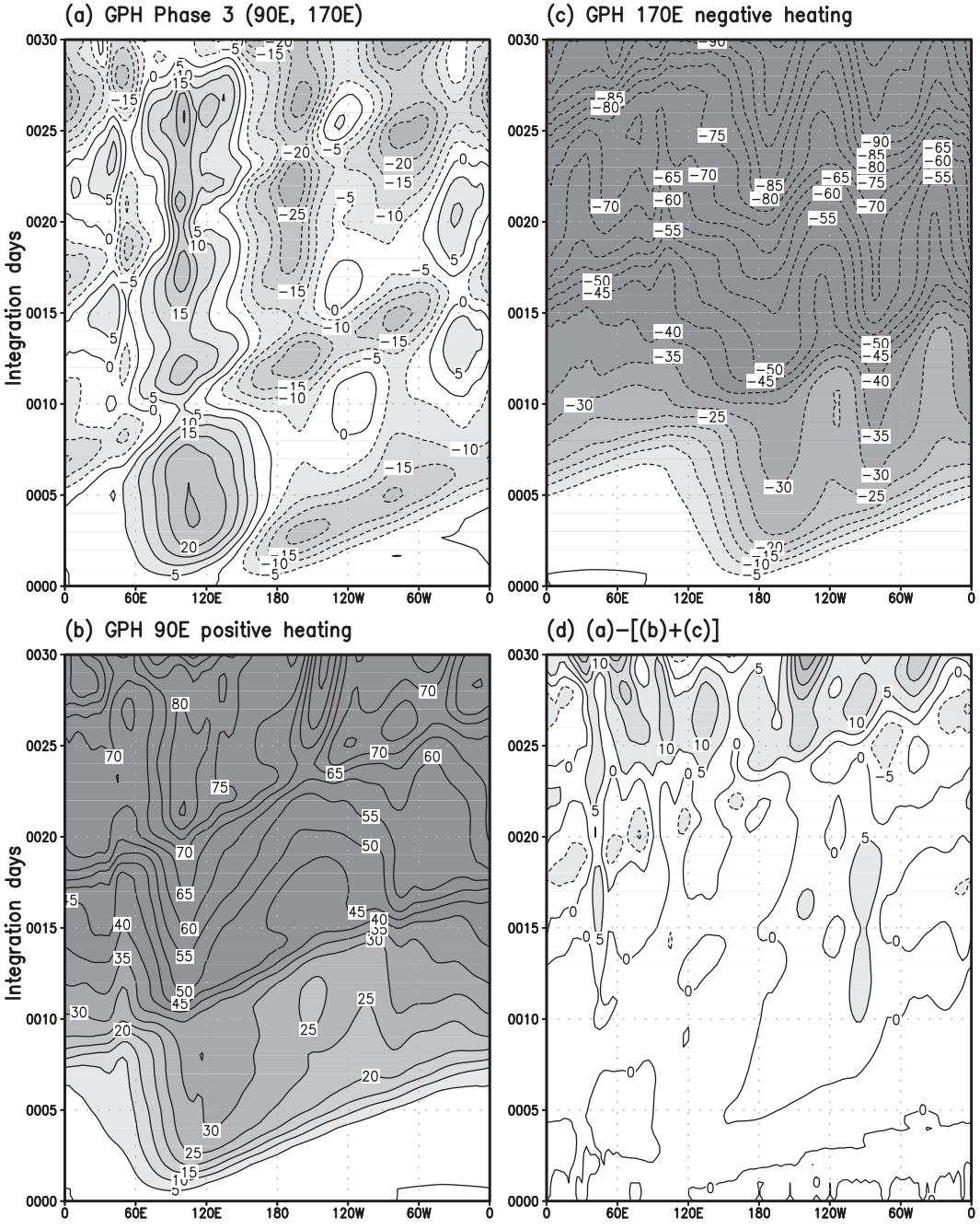

FIG. 7. Time evolution of the upper-troposphere ($\sigma = 0.225$) geopotential height anomalies averaged over 5°S and 5°N for (a) MJO phase-3 forcing (i.e., positive heating at 90°E plus negative heating at 170°E), (b) positive heating at 90°E only, (c) negative heating at 170°E only, and (d) the result of (a) − [(b) + (c)].

are a function of meridional location. Then, the group velocities for each direction are expressed as

$$c_{gx} = \frac{\partial \omega}{\partial k} = \overline{U} + \frac{\beta_* (k^2 - l^2)}{K^4} = c + \frac{2\beta_* k^2}{K^4},$$
$$c_{gy} = \frac{\partial \omega}{\partial l} = \frac{2\beta_* kl}{K^4}. \quad (3)$$

The ray of the wave activity, which is represented by group velocity, is calculated by solving the following relations using a fourth-order Runge–Kutta method (Press et al. 1992):

$$\frac{dx}{dt} = c_{gx}, \quad \frac{dy}{dt} = c_{gy}. \quad (4)$$

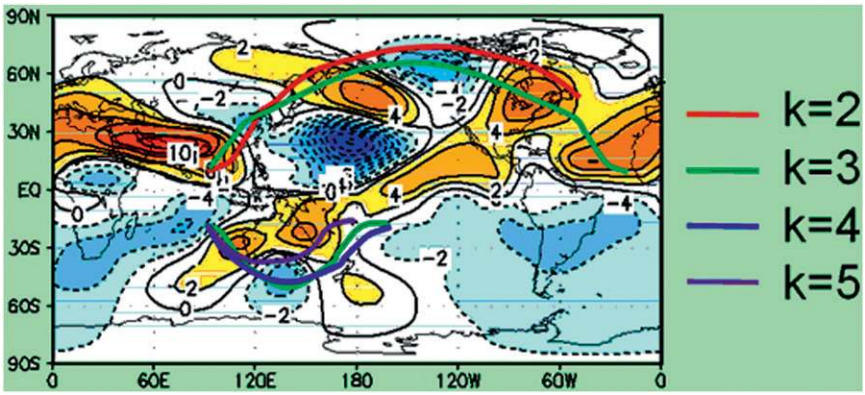

FIG. 8. Rossby ray path computed from the nondivergent barotropic Rossby wave theory for phase-3 forcing; k is the zonal wavenumber. Only the wave train starting from the Indian Ocean is shown for day 15 of model integration. The zonal wavenumbers not shown in the figure are either very short or trapped in the vicinity of the starting point or critical latitude.

Figure 8 illustrates the ray-tracing result for the wave train starting from the Indian Ocean at phase 3. It can be seen that only the waves with zonal wavenumbers 2 and 3 in the NH survive. The wave activity is directed northeastward until it reaches a turning latitude, where $l = 0$. It is then redirected southeastward, taking a great circle–like route. Following the paths of these zonal wavenumbers 2 and 3, the meridional wavenumber, computed from the above dispersion relationship [(2)], varies from 8 to 0 and then to −8 (minus indicates southward propagation). The longer wave (zonal wavenumber 2) propagates more to the north than wavenumber 3, consistent with the Rossby wave dispersion theory. These wave trains are reasonably well matched with the simulated anomaly centers. Furthermore, the wave activity for the zonal wavenumber 3 propagates back to the tropics after the turning latitude is met, ultimately depositing the wave energy in the regions of the tropical Atlantic Ocean and West Africa. Consequently, the tropical circulation anomalies in these regions are formed by the combined effects of the tropically trapped Rossby and Kelvin waves and the meridionally propagating Rossby wave train activity. By contrast, in the SH the shorter waves with zonal wavenumbers 3, 4, and 5 make a short counterclockwise journey since they quickly reach a critical latitude at which the zonal phase speed is equal to the basic zonal flow or the meridional wave scale tends to zero (i.e., l or K goes to infinity). In both hemispheres, wave activity for the other zonal wavenumbers is trapped or dissipated. Based on these results, it is concluded that the global circulation anomalies associated with MJO forcing mainly arise from the equatorially trapped Rossby and Kelvin waves, meridionally propagating Rossby wave and their interaction in the subtropics.

d. Rossby wave source

To better understand the development of circulation response in the extratropics, the RWS is examined using the following linearized forced barotropic vorticity equation (Sardeshmukh and Hoskins 1988):

$$\frac{\partial \zeta'}{\partial t} + \overline{\mathbf{v}}_\psi \cdot \nabla \zeta' + \mathbf{v}'_\psi \cdot \nabla \overline{\zeta} = S' + F', \tag{5}$$

where ζ is the absolute vorticity and $\mathbf{v}_\psi$ is the rotational velocity vector. Also, S denotes the RWS, and F is the frictional term and is considered negligible. The overbar represents the basic flow and the prime the perturbation. The perturbation RWS S' is expressed as follows:

$$S' = -\overline{\zeta}\nabla \cdot \mathbf{v}'_\chi - \mathbf{v}'_\chi \cdot \nabla \overline{\zeta} - \zeta' \nabla \cdot \overline{\mathbf{v}}_\chi - \overline{\mathbf{v}}_\chi \cdot \nabla \zeta', \tag{6}$$

where $\mathbf{v}_\chi$ is the divergence velocity vector. This equation indicates that RWS depends on the relative position and importance of divergence and absolute vorticity fields. The first and second terms on the right-hand side of (6) represent the generation of wave vorticity by the horizontal divergence due to the perturbation divergent winds and the advection of mean absolute vorticity by the perturbation divergent winds, respectively. The third and fourth terms represent the generation of wave vorticity by divergence of the divergent basic winds and the advection of perturbation absolute vorticity by the divergent basic winds, respectively. Each term in (6) can be calculated using observations, but this does not provide clear insights into the role of S' (and its related process) since observations are an end result and contain complicated, small-scale, perturbation wave source/sink patterns. Hence, the above quantities are calculated for the

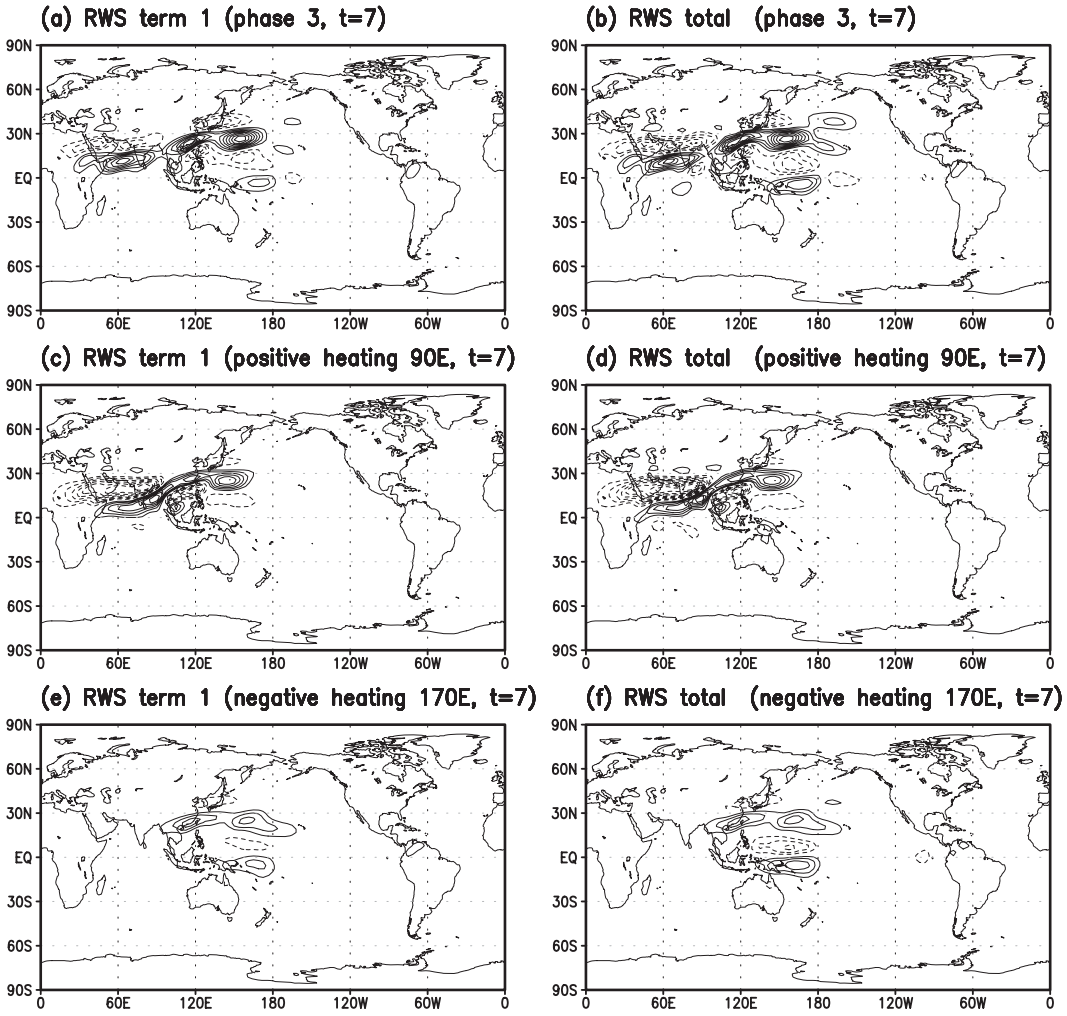

FIG. 9. Perturbation Rossby wave source S' at $\sigma = 0.225$ at day 7 of the model simulation with (a),(b) MJO phase-3 forcing, (c),(d) positive heating at 90°E only, and (e),(f) negative heating at 170°E only, showing (left) the first and (right) the total term in (6). The contour interval is 0.75×10^{-11} s^{-2}. Zero contours are suppressed, and solid (dotted) lines denote positive (negative) perturbations.

day-7 model integrations at the upper level ($\sigma = 0.225$). An exponential spectral filter of the form $e^{-K[n(n+1)]^2}$ is applied to smooth the perturbation RWS fields as in Sardeshmukh and Hoskins (1984). In this filter, K is chosen such that the highest wavenumber spectral coefficients are multiplied by 0.1 as in Sardeshmukh and Hoskins (1984) and Lin (2009).

Figure 9 shows S' at day 7 for the first and total terms in (6) for the dipole heating case of phase 3, only positive heating at 90°E, and only negative heating at 170°E. It is evident that S' is dominated by the first term, indicating that the upper-level perturbation divergent flow dominantly contributes to the wave source. This fact holds for the circulation response to tropical monopole heating as presented in Sardeshmukh and Hoskins (1988) and even to the Asian summer monsoon–related diabatic heating as shown in Lin (2009). The S' shown in Fig. 9b are formed closely in relation to the forced heating and cooling; for example, at the locations of these forcings (i.e., the equatorial Indian Ocean and western Pacific), positive and negative S' develop along the equator, respectively, and the abundant S' with an opposite sign appear farther north. Along the Asian–Pacific jet, S' is also formed from the interaction of the divergent perturbations forced by the tropical heating and the large relative vorticity near the jet stream that acts as a waveguide (Hoskins and Ambrizzi 1993). In contrast to the NH, S' values in the SH are considerably weak and confined just south of the forcing centers, which explains the limited wave dispersion in the SH, as shown in Fig. 6. Although not shown, this hemispheric asymmetry in S' results from a much deeper latitudinal extent of the background easterlies

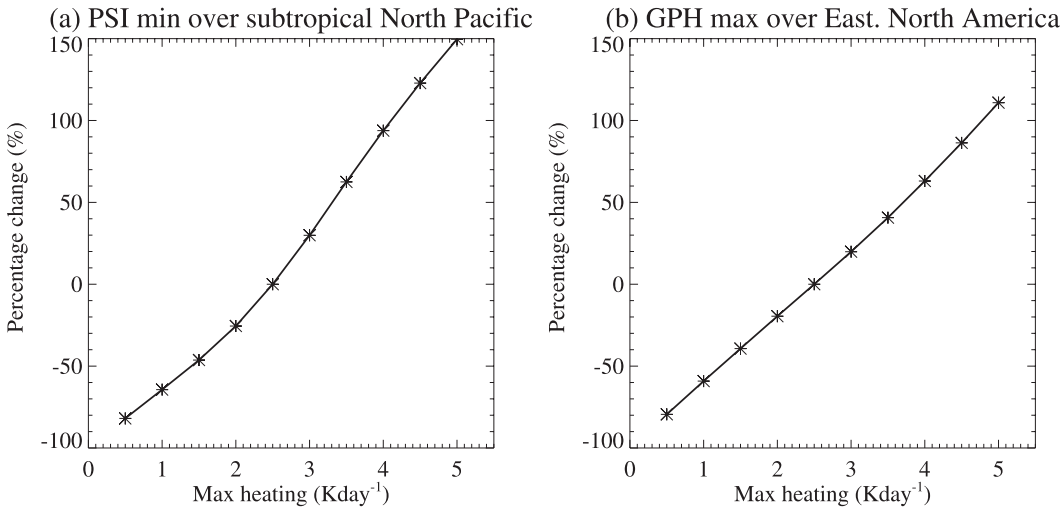

FIG. 10. The percentage change of the (a) minimum streamfunction anomaly over the subtropical North Pacific (0°–30°N, 120°E–120°W), and (b) maximum geopotential anomaly over eastern North America (30°–60°N, 60°–110°W) as a function of maximum heating (K day^{-1}) for MJO phase-3 forcing. The percentage change is with respect to the maximum heating of 2.5 K day^{-1}.

(up to about 18°S) in the SH tropics and a much weaker jet in the midlatitudes. This region corresponds to the negative absolute vorticity gradient. According to the linear theory of a nondivergent barotropic Rossby wave, the waves becomes evanescent there (e.g., Hoskins and Ambrizzi 1993; Matthews and Kiladis 1999).

The RWS associated with monopole forcing over the Indian Ocean and the western Pacific are shown in Figs. 9c–f. Again S' is dominated by the first term in both experiments. However, overall distribution of S' is quite different between the two experiments. The monopole heating at 90°E generates much broader and stronger S' than the monopole cooling at 170°E. It suggests that strong positive S' over the subtropical western Pacific (15°–30°N, 120°E–180°) in Fig. 9b is mainly due to the heating over the Indian Ocean (Fig. 9d). This is why the Rossby wave paths, starting from the Indian Ocean as shown in Fig. 8, have a tendency to mimic the streamfunction anomaly patterns with a great degree of fidelity. In addition, it explains why the formation of the Rossby wave train is dependent on the longitudinal location of the external forcing relative to the zonally asymmetric basic zonal wind pattern.

e. Model sensitivity tests

In this section, the sensitivity of model results to heating structure and basic state is investigated. First, the amplitude of heating is varied from 0.5 to 5.0 K day^{-1} with no change in the shape of heating profile. Figure 10 shows the percentage change of circulation amplitudes at the subtropical North Pacific and eastern North America. These two locations are chosen to represent the localized minimum and maximum streamfunction anomalies, respectively, in the NH extratropics (see Fig. 4g). It is evident that the amplitude of the circulation response increases quasi-linearly with heating amplitude. It confirms the conjecture that the circulation response in our experiments is essentially linear to the imposed MJO-like forcing.

The sensitivity to the heating profile is also investigated by changing vertical gradient of heating. An increase or decrease in the heating gradient about the maximum heating level does not result in appreciable changes in the circulation responses (not shown). This is also the case for the change of the maximum heating level. A shallower heating peak reduces the circulation response in the upper levels (because of the decreased heating itself) but enhances the circulation response in the lower levels (because of increased heating), but the patterns of the response are nearly identical (not shown). In addition, a variety of horizontal diffusion coefficients are applied to the model integrations. Tests with a broad range of fourth-order horizontal diffusion coefficients ($1–10 \times 10^{16}$ m^4 s^{-1}), which includes the coefficient value (2.33×10^{16} m^4 s^{-1}) used in Jin and Hoskins (1995), have only produced negligible differences in the circulation pattern (not shown). It is hence concluded that model results presented in the previous sections are insensitive to the forcing structure and dissipation scheme.

The sensitivity to the basic states is also investigated by changing climatological background flow. Instead of the DJF climatology, basic states of the El Niño and La Niña years are employed. The El Niño and La Niña years are selected according to NCEP Climate Prediction

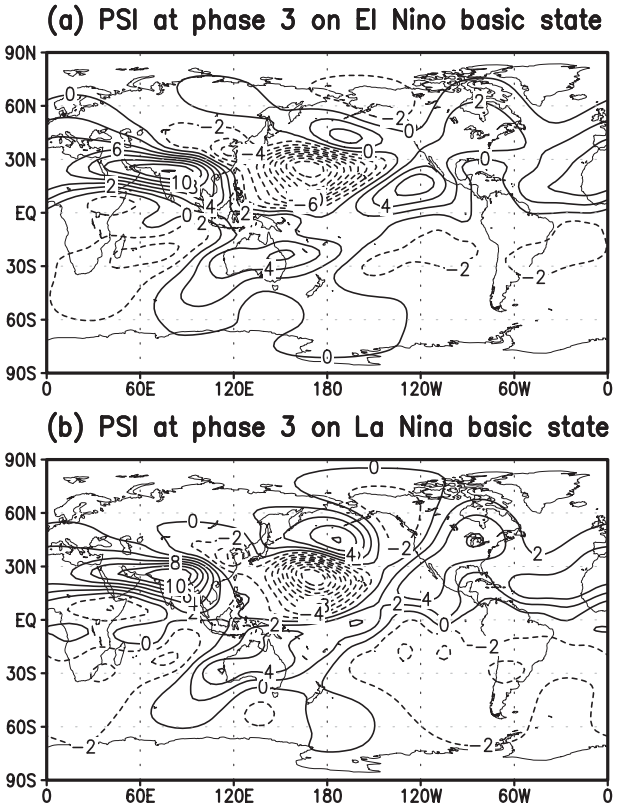

FIG. 11. Response of upper-troposphere (σ = 0.225) streamfunction to MJO phase-3 forcing at day 15 for the (a) El Niño and (b) La Niña 3D basic states. Selected El Niño years are 1982/83, 1986/87, 1991/92, 1994/95, 1997/98, and 2002/03 and selected La Niña years are 1988/89, 1995/96, 1998/99, and 2000/01.

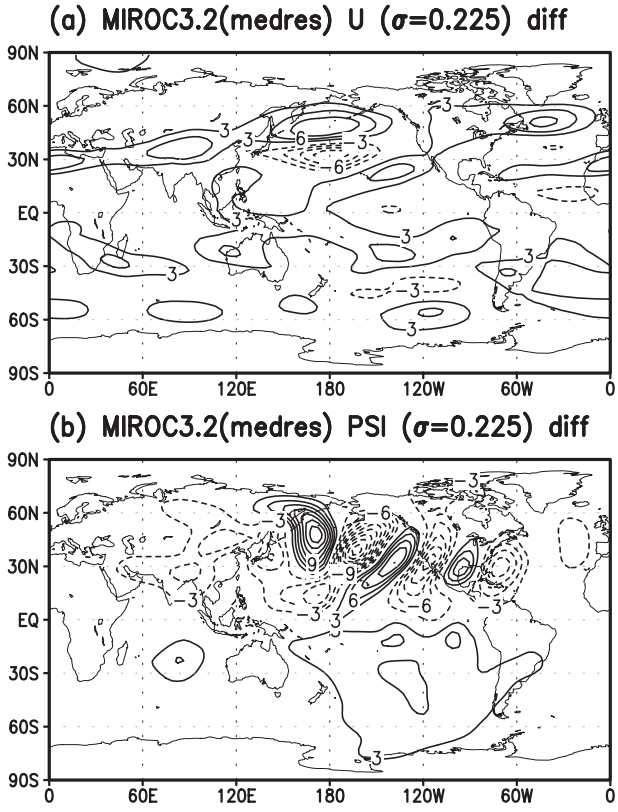

FIG. 12. (a) Mean zonal wind difference at σ = 0.225 (with an interval of 3 m s^{-1}) between 2091–2100 and 2001–10, and (b) day-15 upper-troposphere (σ = 0.225) streamfunction anomaly difference between 2091–2100 and 2001–10 (with an interval of 3.0 × 10^6 m^2 s^{-1}) at phase 3 in the MIROC3.2 (medres) twenty-first-century (21C) A2 scenario simulation.

Center criteria and their basic states are arithmetic averages of the DJF wind, temperature, and surface pressure fields. Figures 11a and 11b show upper-troposphere streamfunction anomaly at day 15 for the El Niño and La Niña basic states. The observed MJO convections during El Niño years are known to propagate farther to the east (crossing the date line) than a normal year (Kessler 2001), whereas those during La Niña years are typically retracted to the western Pacific (Lau and Waliser 2005). Despite this difference in MJO convections, the same forcing is applied to both El Niño– and La Niña–year flows to isolate the role of the basic state, as in Matthews et al. (2004). The gross features in both experiments appear similar to those of the reference case (Fig. 4g). However, for both basic states (Figs. 11a,b), the cyclonic anomaly over Alaska and anticyclonic anomaly over North America are weakened, whereas the cyclonic anomaly over the tropical Pacific is strengthened. In addition, the cyclonic anomaly over tropical Pacific is somewhat strengthened and the SH circulation responses are generally weakened. Under the El Niño basic state, the anticyclonic anomaly over the tropical eastern Pacific is strengthened (Fig. 11a). Use of the El Niño Modoki or central Pacific–El Niño basic state (Ashok et al. 2007a; Yeh et al. 2009) also shows similar properties to the response to the El Niño basic state (not shown). These results suggest that the response of the extratropical circulations to the MJO forcing is moderately sensitive to the background flow and would vary on interannual to decadal time scales.

Finally, possible changes in circulation response to the MJO forcing in a warm climate are examined. The A2 scenario integration of the Model for Interdisciplinary Research on Climate, version 3.2 with medium-resolution [MIROC3.2 (medres)], one of the IPCC AR4 models, is selected and the 3D basic states are computed by averaging for 2001–10 and 2091–2100 separately. It is expected that the anthropogenic warming will tend to increase the SST and thus the strength of the MJO convection. However, to determine the impact of background flow change in a warm climate, the original MJO forcing in Figs. 2 and 3 is applied as in the experiments with El Niño and La Niña basic states. Figure 12a shows the difference in upper-troposphere zonal wind between

2090–2100 and 2001–10. In general, IPCC climate models predict that the jet streams move poleward in response to greenhouse gas forcing (Meehl et al. 2007). This can be seen in the MIROC3.2 A2 scenario simulation with peculiar northward intensification at the exit region of the Asian–Pacific jet. The Atlantic and Mediterranean jet streams are also intensified but with no significant meridional displacement. Figure 12b shows the day-15 upper-troposphere ($\sigma = 0.225$) streamfunction anomaly difference in model simulations with 2091–2100 and 2001–10 climatologies. A significant difference is found over the northern Pacific and North America, which may be related to the generation of more Rossby wave activity at the jet exit and its downstream regions. Although not shown, qualitatively similar results are also found in the simulation with the third climate configuration of the Met Office Unified Model (HadCM3) climatology. Here it should be noted that circulation response would be even stronger if one considers that MJO forcing in a warm climate would be strengthened in the future.

4. Summary

The MJO accounts for a large fraction of the upper-troposphere global circulation variability on an intraseasonal time scale. Therefore, the MJO convective anomalies and related circulation response should be realistically simulated in climate models to enhance the predictability of weather and climate in both the tropics and the extratropics. In this study, the linear response of the atmospheric circulations to the MJO heating is extensively examined by performing a series of initial-value calculations. More specifically, a dynamical core GCM is integrated by forcing an idealized thermal heating/cooling on the climatological boreal winter background flow. Although simulated global circulation response to the MJO-like forcing is essentially linear, it resembles the observed circulation anomalies very well, especially for the MJO phase 3.

It is found that the tropical circulation anomalies characterized by a cyclonic or anticyclonic flow couplet about the equator are created as a forced equatorial Rossby and Kelvin wave response to the MJO heating. Since Kelvin waves are about 3 times faster than Rossby waves and these waves propagate in the opposite direction, the circulation anomalies induced from the MJO-like dipole heating (heating and cooling) tend to either interfere with or intensify each other, resulting in a dramatically different circulation response in the tropics from the experiments with only monopole heating or cooling. For instance, westward-propagating anomalies in the form of Rossby waves to the west of the heating are opposed by the opposite-signed anomalies produced by eastward-encircling Kelvin waves to the east of the cooling.

The modeled extratropical circulation anomalies well match the observed wavelike structures and successive downstream development of new centers of action, indicating that they also arise from a direct response to the MJO heating and the interaction of the divergent perturbations forced by the tropical heating and the large relative vorticity basic field near the jet stream. A wave activity tracing using the Rossby wave dispersion theory shows that Rossby wave trains to the extratropics are formed by the large-scale waves with zonal wavenumbers 2–3 and 3–5 in the NH and SH, respectively. They are generated by the MJO heating over the Indian Ocean, propagate northeastward in the NH until meeting a turning latitude, and return back to the equator and deposit their energy over the tropical Atlantic and West Africa (see zonal wavenumber 3 in Fig. 8). It intensifies the amplitude of circulation anomalies there that are initially formed by the zonally propagating equatorial Rossby and Kelvin waves. As such, the amplitude of the circulation anomalies over those regions in the NH is larger than the southern counterpart. Interestingly, if this happens also in the summer, the above feeding process could affect the triggering and growth of tropical cyclones and hurricanes. It will be investigated in a future study.

The Rossby wave source (RWS) calculations further revealed that divergent flow in the upper troposphere, generated by MJO heating, plays a dominant role in the generation of wave vorticity. The realistic dipole forcing (MJO phase 3) experiment is compared with the monopole forcing experiments. The summation of the resulting RWS by the two monopole forcing experiments (i.e., Figs. 9d,f) produces an RWS pattern and magnitude similar to those generated by the dipole forcing (Fig. 9b), implying a linear property in the formation of wave vorticity by MJO-like forcing. It is also found that spatial scales of the RWS in the two monopole heating experiments are quite different. The heating over the Indian Ocean generates much broader and stronger RWS because of its position relative to the Asian–Pacific jet, where the relative vorticity is large. It suggests that the strong cyclonic and anticyclonic dipole over the North Pacific at the date line (Fig. 4g) is mainly caused by the Rossby waves forced by the heating over the Indian Ocean and the ensuing interaction of these waves with the mean flow (i.e., the jet and its relative vorticity), although the cooling over the western Pacific also contributes to the circulation anomaly.

The above results are found to be insensitive to detailed structure of tropical heating and diffusion coefficients. It is, however, found that the global circulation response to the MJO-like forcing shows nonnegligible sensitivity to

the 3D basic state (i.e., long-term climatology, El Niño and La Niña basic states). The circulation response to MJO forcing under the future warm climate is also examined. For the A2 scenario future climate integration of the MIROC3.2 (medres) that produces peculiar northward intensification of the Asian-Pacific jet at its exit region, it shows a pronounced change in the circulation responses over the northern Pacific and North America, which may be related to the generation of more Rossby wave activity over the jet exit and its downstream regions.

This study presents that the MJO-related diabatic heatings over the Indian and western Pacific Oceans can directly affect the global circulation by exciting equatorially trapped Rossby and Kelvin waves in the tropics, Rossby wave train from the deep tropics to the extratropics over the central North Pacific and its vicinity, and their interactions over the subtropical North Atlantic. This result suggests that, to better predict global circulation anomalies during the boreal winter, the MJO should be reasonably well simulated and forecasted in the numerical weather and climate forecast models. It should be noted that in this study we focus on the linear response of the atmospheric circulation to the prescribed MJO-like forcing. However, the nonlinearity—such as that associated with interaction between the convectively driven equatorial and midlatitude waves (e.g., Majda and Biello 2003) or two-way interaction between the forcing and background flow—would play an important role in the extratropics. This is particularly true during MJO phases 1 and 4 (Figs. 4e,h; see the lower pattern correlations for 30°–90°N in Table 1). This nonlinearity will be addressed in a future study by integrating the same model with time-varying background flow as in Lin (2009).

Acknowledgments. This work was supported by the National Research Foundation of Korea (NRF) Grant (2011-0015486) funded by the Korean government (the Ministry of Education, Science and Technology). We thank Dr. Shigeo Yoden and the anonymous reviewers for their constructive comments. The authors acknowledge the support of the Korea Institute of Science and Technology Information (KISTI).

REFERENCES

Ashok, K., S. Behera, A. S. Rao, H. Weng, and T. Yamagata, 2007a: El Niño Modoki and its teleconnection. *J. Geophys. Res.,* **112,** C11007, doi:10.1029/2006JC003798.

——, H. Nakamura, and T. Yamagata, 2007b: Impacts of ENSO and Indian Ocean dipole events on the Southern Hemisphere storm-track activity during austral winter. *J. Climate,* **20,** 3147–3163.

Borges, M. D., and P. D. Sardeshmukh, 1995: Barotropic Rossby wave dynamics of zonally varying upper-level flows during northern winter. *J. Atmos. Sci.,* **52,** 3779–3796.

Branstator, G., 1983: Horizontal energy propagation in a barotropic atmosphere with meridional and zonal structure. *J. Atmos. Sci.,* **40,** 1689–1708.

Derbyshire, S. H., I. Beau, P. Bechtold, J.-Y. Grandpeix, J.-M. Piriou, J.-L. Redelsperger, and P. M. M. Soares, 2004: Sensitivity of moist convection to environmental humidity. *Quart. J. Roy. Meteor. Soc.,* **130,** 3055–3079.

Ebisuzaki, W., 1997: A method to estimate the statistical significance of a correlation when the data are serially correlated. *J. Climate,* **10,** 2147–2153.

Fu, X., and B. Wang, 2009: Critical roles of the stratiform rainfall in sustaining the Madden–Julian oscillation: GCM experiments. *J. Climate,* **22,** 3939–3959.

——, B. Yang, G. Bao, and B. Wang, 2008: Sea surface temperature feedback extends the predictability of tropical intraseasonal oscillation. *Mon. Wea. Rev.,* **136,** 577–597.

Gill, A. E., 1980: Some simple solutions for heat-induced tropical circulation. *Quart. J. Roy. Meteor. Soc.,* **106,** 447–462.

Gordon, C. T., and W. F. Stern, 1982: A description of the GFDL global spectral model. *Mon. Wea. Rev.,* **110,** 625–644.

Hendon, H. H., 2000: Impact of air–sea coupling on the Madden–Julian oscillation in a general circulation model. *J. Atmos. Sci.,* **57,** 3939–3952.

Higgins, R. W., J.-K. E. Schemm, W. Shi, and A. Leetmaa, 2000: Extreme precipitation events in the western United State related to tropical forcing. *J. Climate,* **13,** 793–820.

Hoskins, B. J., and D. J. Karoly, 1981: The steady linear response of a spherical atmosphere to thermal and orographic forcing. *J. Atmos. Sci.,* **38,** 1179–1196.

——, and T. Ambrizzi, 1993: Rossby wave propagation on a realistic longitudinally varying flow. *J. Atmos. Sci.,* **50,** 1661–1671.

Inness, P. M., and J. M. Slingo, 2003: Simulation of the Madden–Julian oscillation in a coupled general circulation model. Part II: The role of the basic state. *J. Climate,* **16,** 365–382.

Jin, F., and B. J. Hoskins, 1995: The direct response to tropical heating in a baroclinic atmosphere. *J. Atmos. Sci.,* **52,** 307–319.

Jones, C., and J.-K. E. Schemm, 2000: The influence of intraseasonal variations on medium- to extended-range weather forecasts over South America. *Mon. Wea. Rev.,* **128,** 486–494.

Kalnay, E., and Coauthors, 1996: The NCEP/NCAR 40-Year Reanalysis Project. *Bull. Amer. Meteor. Soc.,* **77,** 437–471.

Karoly, D. J., 1983: Rossby wave propagation in a barotropic atmosphere. *Dyn. Atmos. Oceans,* **7,** 111–125.

Kessler, W. S., 2001: EOF representation of the Madden–Julian oscillation and its connection with ENSO. *J. Climate,* **14,** 3055–3061.

Kuang, Z., 2008: A moisture-stratiform instability for convectively coupled waves. *J. Atmos. Sci.,* **65,** 834–854.

Lau, K.-M., and D. E. Waliser, 2005: *Intraseasonal Variability in the Atmosphere–Ocean Climate System*. Springer Praxis, 474 pp.

Liebmann, B., and C. A. Smith, 1996: Description of a complete (interpolated) outgoing longwave radiation dataset. *Bull. Amer. Meteor. Soc.,* **77,** 1275–1277.

Lin, H., 2009: Global extratropical response to diabatic heating variability of the Asian summer monsoon. *J. Atmos. Sci.,* **66,** 2697–2713.

Lin, J.-L., B. Mapes, M. Zhang, and M. Newman, 2004: Stratiform precipitation, vertical heating profiles, and the Madden–Julian oscillation. *J. Atmos. Sci.,* **61,** 296–309.

——, and Coauthors, 2006: Tropical intraseasonal variability in 14 IPCC AR4 climate models. Part I: Convective signals. *J. Climate,* **19,** 2665–2690.

Madden, R. A., and P. R. Julian, 1972: Description of global-scale circulation cells in the tropics with a 40–50 day period. *J. Atmos. Sci.,* **29,** 1109–1123.

Majda, A. J., and J. A. Biello, 2003: The nonlinear interaction of barotropic and equatorial baroclinic Rossby waves. *J. Atmos. Sci.,* **60,** 1809–1821.

Mapes, B. E., 2000: Convective inhibition, subgrid-scale triggering energy, and stratiform instability in a toy tropical wave model. *J. Atmos. Sci.,* **57,** 1515–1535.

Matthews, A. J., 2000: Propagation mechanisms for the Madden–Julian oscillation. *Quart. J. Roy. Meteor. Soc.,* **126,** 2637–2651.

——, and G. N. Kiladis, 1999: Interactions between ENSO, transient circulation, and tropical convection over the Pacific. *J. Climate,* **12,** 3062–3086.

——, B. J. Hoskins, and M. Masutani, 2004: The global response to tropical heating in the Madden–Julian oscillation during the northern winter. *Quart. J. Roy. Meteor. Soc.,* **130,** 1911–2011.

Meehl, G. A., and Coauthors, 2007: Global climate projections. *Climate Change 2007: The Physical Science Basis,* S. Solomon et al., Eds., Cambridge University Press, 747–845.

Moorthi, S., and M. J. Suarez, 1992: Relaxed Arakawa-Schubert: A parameterization of moist convection for general circulation models. *Mon. Wea. Rev.,* **120,** 978–1002.

——, and ——, 1999: Documentation of version 2 of relaxed Arakawa–Schubert cumulus parameterization with convective downdrafts. NOAA Office Note 99-01, 44 pp.

Press, W. H., S. A. Teukolsky, W. Y. Vetterling, and B. P. Flannery, 1992: *Numerical Recipes in Fortran 77: The Art of Scientific Computing*. Cambridge University Press, 931 pp.

Sardeshmukh, P. D., and B. J. Hoskins, 1984: Spatial smoothing on the sphere. *Mon. Wea. Rev.,* **112,** 2524–2529.

——, and ——, 1988: The generation of global rotational flow by steady idealized tropical divergence. *J. Atmos. Sci.,* **45,** 1228–1251.

Seo, K.-H., and K.-Y. Kim, 2003: Propagation and initiation mechanisms of the Madden-Julian oscillation. *J. Geophys. Res.,* **108,** 4384, doi:10.1029/2002JD002876.

——, and W. Wang, 2010: The Madden–Julian oscillation simulated in the NCEP Climate Forecast System model: The importance of stratiform heating. *J. Climate,* **23,** 4770–4793.

——, J.-K. Schemm, C. Jones, and S. Moorthi, 2005: Forecast skill of the tropical intraseasonal oscillation in the NCEP GFS dynamical extended range forecasts. *Climate Dyn.,* **25,** 265–284.

——, J.-K. E. Schemm, W. Wang, and A. Kumar, 2007: The boreal summer intraseasonal oscillation simulated in the NCEP Climate Forecast System (CFS): The effect of sea surface temperature. *Mon. Wea. Rev.,* **135,** 1807–1827.

——, W. Wang, J. Gottschalck, Q. Zhang, J.-K. E. Schemm, W. R. Higgins, and A. Kumar, 2009: Evaluation of MJO forecast skill from several statistical and dynamical forecast models. *J. Climate,* **22,** 2372–2388.

Slingo, J. M., and Coauthors, 1996: Intraseasonal oscillations in 15 atmospheric general circulation models: Results from an AMIP diagnostic subproject. *Climate Dyn.,* **12,** 325–357.

Son, S.-W., and S. Lee, 2005: The response of westerly jets to thermal driving in a primitive equation model. *J. Atmos. Sci.,* **62,** 3741–3757.

Sperber, K. R., S. Gualdi, S. Legutke, and V. Gayler, 2005: The Madden–Julian oscillation in ECHAM4 coupled and uncoupled general circulation models. *Climate Dyn.,* **25,** 117–140.

Ting, M., and I. M. Held, 1990: The stationary wave response to a tropical SST anomaly in an idealized GCM. *J. Atmos. Sci.,* **47,** 2546–2566.

Wheeler, M., and H. H. Hendon, 2004: An all-season real-time multivariate MJO index: Development of an index for monitoring and prediction. *Mon. Wea. Rev.,* **132,** 1917–1932.

Yeh, S.-W., J.-S. Kug, B. Dewitte, M.-H. Kwon, B. P. Kirtman, and F.-F. Jin, 2009: El Niño in a changing climate. *Nature,* **461,** 511–514.